

How much can ^{56}Ni be synthesized by the magnetar model for long gamma-ray bursts and hypernovae?

Yudai Suwa^{1,2★} and Nozomu Tominaga^{3,4}

¹*Yukawa Institute for Theoretical Physics, Kyoto University, Oiwake-cho, Kitashirakawa, Sakyo-ku, Kyoto, 606-8502, Japan*

²*Max-Planck-Institut für Astrophysik, Karl-Schwarzschild-Str. 1, D-85748 Garching, Germany*

³*Department of Physics, Faculty of Science, and Engineering, Konan University, 8-9-1 Okamoto, Kobe, Hyogo 658-8501, Japan*

⁴*Kavli Institute for the Physics, and Mathematics of the Universe (WPI), University of Tokyo, Kashiwa, Chiba 277-8583, Japan*

Accepted 2015 April 20. Received 2015 April 14; in original form 2015 February 10

ABSTRACT

A rapidly rotating neutron star with strong magnetic fields, called a magnetar, is a possible candidate for the central engine of long gamma-ray bursts and hypernovae (HNe). We solve the evolution of a shock wave driven by the wind from a magnetar and we evaluate the temperature evolution, by which we estimate the amount of ^{56}Ni that produces the bright emission of HNe. We obtain a constraint on the magnetar parameters (i.e. the poloidal magnetic field strength B_p and initial angular velocity Ω_i) for synthesizing enough ^{56}Ni mass to explain HNe ($M_{^{56}\text{Ni}} \gtrsim 0.2 M_\odot$), that is, $(B_p/10^{16} \text{ G})^{1/2} (\Omega_i/10^4 \text{ rad s}^{-1}) \gtrsim 0.7$.

Key words: gamma-ray burst: general – stars: magnetars – supernovae: general – stars: winds, outflows.

1 INTRODUCTION

The central engine of gamma-ray bursts (GRBs) is still unknown despite a wealth of observational data. The most popular scenario for a subclass with long duration (a long GRB) is the collapsar scenario (Woosley 1993), which contains a black hole and a hyper accretion flow; an alternative scenario is a rapidly rotating neutron star (NS) with strong magnetic fields (i.e. the magnetar scenario; Usov 1992). The energy budgets are determined by the gravitational binding energy of the accretion flow for the former scenario and the rotational energy of a NS for the latter scenario.

On the other hand, the association between long GRBs and energetic supernovae, called hypernovae (HNe), has been observationally established since GRB 980425/SN 1998bw and GRB 030329/SN 2003dh (see Woosley & Bloom 2006; Hjorth & Bloom 2012, and references therein). The explosion must involve at least two components: a relativistic jet, which generates a GRB, and more spherical-like non-relativistic ejecta, observed as a HN. One of observational characteristics of HNe is high peak luminosity; HNe are typically brighter by $\sim 1\text{--}2$ mag than canonical supernovae. The brightness of HNe stems from an ejection of a much larger amount of ^{56}Ni ($0.2\text{--}0.5 M_\odot$; Nomoto et al. 2006) than canonical supernovae ($\lesssim 0.1 M_\odot$; e.g. Blinnikov et al. 2000 for SN 1987A).

Mechanisms that generate such a huge amount of ^{56}Ni by a HN have been investigated (e.g. MacFadyen & Woosley 1999;

Nakamura et al. 2001a,b; Maeda et al. 2002; Nagataki, Mizuta & Sato 2006; Tominaga et al. 2007; Maeda & Tominaga 2009). They demonstrated that a large amount of ^{56}Ni can be synthesized by explosive nucleosynthesis due to the high explosion energy of a HN and/or be ejected from the accretion disc via disc wind. However, no study on the ^{56}Ni mass for the magnetar scenario has been done so far. The dynamics of the outflow from the magnetar is investigated in detail and it is suggested that the energy release from the magnetar could explain the high explosion energy of HNe (e.g. Thompson, Chang & Quataert 2004; Komissarov & Barkov 2007; Dessart et al. 2008; Bucciantini et al. 2009; Metzger et al. 2011). Not only the explosion dynamics, but also the self-consistent evolutions of magnetized iron cores have been investigated for more than four decades (e.g. LeBlanc & Wilson 1970; Meier et al. 1976; Symbalisty 1984; Burrows et al. 2007; Winteler et al. 2012; Sawai, Yamada & Suzuki 2013; Mösta et al. 2014; Nishimura, Takiwaki & Thielemann 2015), in which magnetohydrodynamic (MHD) equations were solved. In these simulations, rapidly rotating [$P \sim O(1)$ s] and strongly magnetized ($B \sim 10^{9\text{--}12}$ G) cores are employed as initial conditions. The final outcomes after the contraction of cores to NSs are very rapidly rotating [$P \sim O(1)$ ms] and very strongly magnetized ($B \sim 10^{14\text{--}16}$ G) NSs, which can generate magnetic-driven outflows. These studies, however, basically focused on the shock dynamics affected by strong magnetic fields and/or yield of r-process elements, but have scarcely paid attention to the amount of ^{56}Ni so far. Additionally, these simulations have not been able to produce strong enough explosions to explain HNe, but have tried to explain canonical supernovae (the explosion energy $\sim 10^{51}$ erg; for

★ E-mail: suwa@yukawa.kyoto-u.ac.jp

HNe, $\sim 10^{52}$ erg is necessary). Therefore, there is a need to study the amount of ^{56}Ni generated by the magnetar central engine in order to check the consistency of this scenario.

In this paper, we evaluate the amount of ^{56}Ni by the rapidly spinning magnetar. To do this, we adopt a thin shell approximation and derive an evolution equation of a shock wave driven by the magnetar dipole radiation. The solution of this equation gives the temperature evolution of the post-shock layer. Using the critical temperature (5×10^9 K) for nuclear statistical equilibrium at which ^{56}Ni is synthesized, we give a constraint on the magnetar spin rate and dipole magnetic field strength for explaining the observational amount of ^{56}Ni in HNe. In Section 2, we give expressions for the dipole radiation from a rotating magnetized NS for the central engine model and the derivation of the evolution equation of a shock wave. Based on the solution, we evaluate the temperature evolution and ^{56}Ni mass ($M_{^{56}\text{Ni}}$) as a function of magnetar parameters in Section 3. We summarize our results and discuss their implications in Section 4.

2 COMPUTATIONAL METHOD

According to Shapiro & Teukolsky (1983), the luminosity of dipole radiation is given as

$$L_w = \frac{B_p^2 R^6 \Omega^4 \sin^2 \alpha}{6c^3}, \quad (1)$$

where B_p is the dipole magnetic field strength, R is the NS radius, Ω is the angular velocity, α is the angle between magnetic and angular moments, and c is the speed of light. Hereafter, we assume $\sin \alpha = 1$ for simplicity. Then, the luminosity is expressed as

$$L_w = 6.18 \times 10^{51} \text{ erg s}^{-1} \times \left(\frac{B_p}{10^{16} \text{ G}} \right)^2 \left(\frac{R}{10 \text{ km}} \right)^6 \left(\frac{\Omega}{10^4 \text{ rad s}^{-1}} \right)^4. \quad (2)$$

The time evolution of the angular velocity is given as

$$\Omega(t) = \Omega_i \left(1 + \frac{t}{T_d} \right)^{-1/2}, \quad (3)$$

where Ω_i is the initial angular velocity and T_d is spin-down time-scale given by

$$\begin{aligned} T_d &= \frac{3Ic^3}{B_p^2 R^6 \Omega_i^2} \\ &= 8.08 \text{ s} \left(\frac{B_p}{10^{16} \text{ G}} \right)^{-2} \left(\frac{R}{10 \text{ km}} \right)^{-6} \\ &\quad \times \left(\frac{\Omega_i}{10^4 \text{ rad s}^{-1}} \right)^{-2} \left(\frac{I}{10^{45} \text{ g cm}^2} \right). \end{aligned} \quad (4)$$

Here, I is the moment of inertia of a NS. Therefore, $L_w(t) \propto (1 + t/T_d)^{-2}$. The available energy is the rotation energy of a NS,

$$E_{\text{NS}} = \frac{1}{2} I \Omega_i^2 = 5 \times 10^{52} \text{ erg} \left(\frac{I}{10^{45} \text{ g cm}^2} \right) \left(\frac{\Omega_i}{10^4 \text{ rad s}^{-1}} \right)^2, \quad (5)$$

which corresponds to the total radiation energy $E_w = \int_0^\infty L_w(t) dt = L_w(0) T_d$.

Next, we calculate the time evolution of the shock. For simplicity, we employ thin shell approximation for the ejecta (e.g. Laubach & Probstein 1969; Koo & McKee 1990; Whitworth & Francis 2002).

In this scenario, we consider an isotropic wind, which forms a hot bubble. This bubble sweeps up the surrounding matter into a thin dense shell. This approximation is applicable when the thickness between forward and reverse shocks is small compared to their radii. The comparisons of our solutions with hydrodynamic simulations are shown in the Appendix.

The equation of motion of the shell is given as

$$\frac{d}{dt} (M_s \dot{R}_s) = 4\pi R_s^2 p - F_g, \quad (6)$$

where R_s is the shock radius, M_s is mass of the shell and p is the pressure below the shell, which drives the shell. F_g is the gravitational force, which consists of contributions from a point source ($GM_c M_s / R_s^2$, where G is the gravitational constant and M_c is the mass below the shell) and the self-gravity ($GM_s^2 / 2R_s^2$). \dot{R}_s denotes the derivative of R_s with respect to time. The left-hand side (LHS) represents the increase rate of the outward momentum, while the first term of the right-hand side (RHS) is the driving force of the shell propagation due to the pressure p . We neglect the ram pressure in this model because the ram pressure of the falling matter does not affect the evolution of the shock after the onset (e.g. Tominaga et al. 2007). However, because the ram pressure is highest at the onset of the propagation and influences the onset, we take into account the effect with a condition that the shock propagation time should be shorter than the free-fall time.¹ The ambiguity originating from this approximation is checked by comparing evolutions of shock and temperature with hydrodynamic simulations (see the Appendix).

The energy conservation of the bubble is given as

$$\frac{d}{dt} \left(\frac{4\pi}{3} R_s^3 \frac{p}{\gamma - 1} \right) = L_w - p \frac{d}{dt} \left(\frac{4\pi}{3} R_s^3 \right), \quad (7)$$

where γ is the adiabatic index and L_w is the wind driven by the magnetar, which is assumed to be the dipole radiation given by equation (2). The term on the LHS is the increase rate of the internal energy of the bubble, while terms on the RHS are the energy injection rate by the wind and the power done by the bubble pushing on the shell. Note that it is assumed that the other mechanisms, such as neutrino heating, give no energy to the shock.

Nuclear statistical equilibrium holds and ^{56}Ni is synthesized in a mass shell with the maximum temperature of $> 5 \times 10^9$ K. Thus, the temperature evolution is crucial for the amount of ^{56}Ni . In the following, we consider the post-shock temperature, which is evaluated with the following equation of state,

$$p = p_i + p_e + p_r, \quad (8)$$

where $p_i = n_i k_B T$, $p_e = (7/12) a_{\text{rad}} T^4 [T_9^2 / (T_9^2 + 5.3)]$ and $p_r = a_{\text{rad}} T^4 / 3$ are contributions from ions, non-degenerate electron and positron pairs (Freiburghaus et al. 1999; Tominaga 2009), and radiation, respectively. Here, $n_i = \rho / m_p$ is the ion number density, where m_p is the proton mass and ρ is the density in the shell,² T is the temperature in the shell, $T_9 = (T / 10^9 \text{ K})$, k_B is the Boltzmann

¹ In order to onset the shock propagation, the ram pressure of the falling matter ρv_{ff}^2 is overwhelmed by the thermal pressure p . According to equation (6), the thermal pressure is $p \sim \dot{R}_s M_s / 4\pi R_s^2$ and the ram pressure is $\rho v_{\text{ff}}^2 \sim v_{\text{ff}} \dot{M} / 4\pi R_s^2$, where $\dot{M} \sim 4\pi R_s^2 \rho v_{\text{ff}}$. Thus, the condition is $\dot{R}_s > v_{\text{ff}}$.

² Note that ρ should be different from ρ_0 because matter is compressed by the shock wave. Due to our simple thin shell approximation we need an additional assumption to evaluate ρ . We hereby simply assume that $\rho = \rho_0$, which would lead to higher temperatures. Although the pressure inside the shell might also be different from the one behind the shell, we neglect the difference for simplicity.

constant and $a_{\text{rad}} = 7.56 \times 10^{-15} \text{ erg cm}^{-3} \text{ K}^{-4}$ is the radiation constant. Combined with equation (6), we obtain T in the shell and its evolution is consistent with the shock dynamics.

By substituting equation (6) into equation (7) and eliminating p , we obtain

$$\begin{aligned} & (3\gamma - 4)GM_s(2M_c + M_s)\dot{R}_s + 24\pi\gamma\rho_0 R_s^4 \dot{R}_s^3 \\ & + 8\pi R_s^5 \dot{R}_s (\rho_0' \dot{R}_s^2 + 3\rho_0 \ddot{R}_s) \\ & - 2R_s^2 [3(\gamma - 1)L_w - (3\gamma - 2)M_s \dot{R}_s \ddot{R}_s] \\ & + 2R_s^3 [4\pi G(M_c + M_s)\rho_0 \dot{R}_s + M_s \ddot{R}_s] = 0, \end{aligned} \quad (9)$$

where $\rho_0(r)$ is the density of the progenitor star (i.e. pre-shocked material) and $\rho_0' = d\rho_0/dr$. In this calculation, we used

$$\dot{M}_s = \frac{dM_s}{dt} = \left(\frac{dR_s}{dt} \right) \left(\frac{dM_s}{dR_s} \right) = 4\pi R_s^2 \rho_0(R_s) \dot{R}_s.$$

Note that all mass expelled by the shell is assumed to be accumulated in the shell. For the density structure, ρ_0 , we employ the s40.0 model of Woosley, Heger & Weaver (2002), which is a Wolf-Rayet star with a mass of $8.7 M_\odot$ and a radius of $0.33 R_\odot$. In addition, we use $\gamma = 4/3$. Equation (9) can be written to as a set of first-order differential equations,

$$R_0(t) = R_s(t), \quad (10)$$

$$\dot{R}_0(t) = R_1(t), \quad (11)$$

$$\dot{R}_1(t) = R_2(t), \quad (12)$$

$$\dot{R}_2(t) = f(R_0, R_1, R_2), \quad (13)$$

where

$$\begin{aligned} f(R_0, R_1, R_2) = & -\frac{GR_1}{2M_s R_0^3} \left[(3\gamma - 4)(2M_c + M_s)M_s \right. \\ & \left. + 8\pi R_0^3 \rho_0(M_c + M_s) \right] - \frac{12\pi\gamma}{M_s} \rho_0 R_0 R_1^3 \\ & - \frac{4\pi}{M_s} R_0^2 R_1 (\rho_0' R_1^2 + 3\rho_0 R_2) + \frac{1}{M_s R_0} \\ & \times [3(\gamma - 1)L_w - (3\gamma - 2)M_s R_1 R_2]. \end{aligned} \quad (14)$$

This system of differential equations is integrated using the fourth-order Runge–Kutta time-stepping method. These equations allow us to investigate the shock propagation in the realistic stellar model, which depends on the density structure and the evolution of the energy injection.

3 RESULTS

Fig. 1 presents the time evolutions of shock radius and shock velocity for a constant luminosity of $L_w = 10^{52} \text{ erg s}^{-1}$. Three boundary conditions are needed to solve equation (9) because it is a third-order differential equation. We set R_s , \dot{R}_s and \ddot{R}_s at $t = 0$. Fig. 1 shows models with different initial conditions: models with different injection points $R_s(t = 0) = 1500 \text{ km}$ ($M_c = 1.5 M_\odot$; red thick-solid and green thin-dashed lines) and $R_s(0) = 850 \text{ km}$ ($M_c = M_\odot$; blue thick-dashed and magenta thin-dotted lines), and models with different initial velocity $\dot{R}_s(0) = 0$ (two thick lines) and $\dot{R}_s(0) = v_0 \equiv \sqrt{GM_c/2R_s(0)}$ (two thin lines), that is, velocity necessary to overwhelm ram pressure (see Maeda & Tominaga 2009).

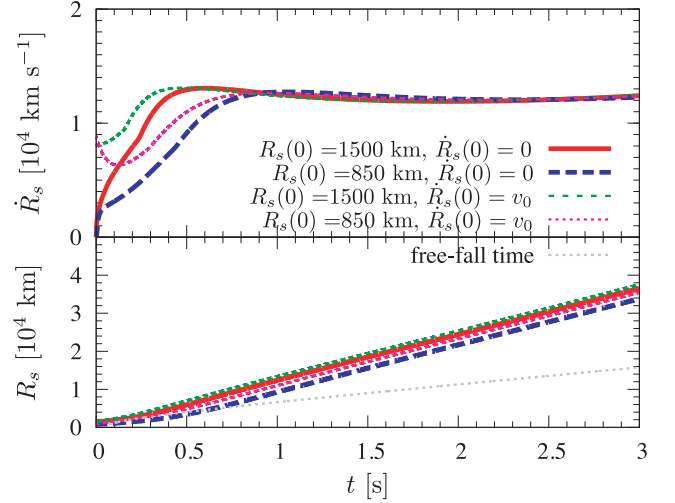


Figure 1. Time evolutions of shock velocity (top panel) and shock radius (bottom panel). Four different lines represent different initial conditions for the shock radius ($R_s(0) = 850$ or 1500 km) and shock velocity ($\dot{R}_s(0) = 0$ or $v_0 = \sqrt{GM_c/2R_s(0)}$). The grey dotted line in the bottom panel represents the free-fall time at each radius.

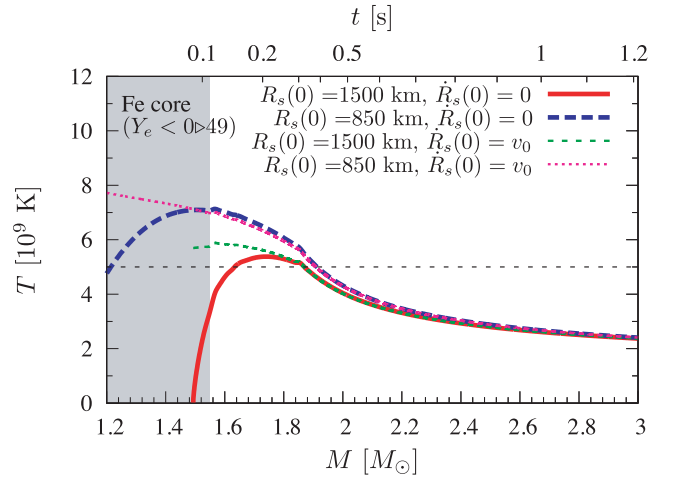


Figure 2. The post-shock temperature as a function of mass coordinate. The model parameters are the same as in Fig. 1. The horizontal dotted line represents $5 \times 10^9 \text{ K}$, above which ^{56}Ni is synthesized. The grey shaded region, $M(r) < 1.55 M_\odot$, is the iron core, where ^{56}Ni cannot be synthesized due to the low electron fraction of $Y_e < 0.49$. The corresponding time of the model with $R_s(0) = 850 \text{ km}$ and $\dot{R}_s(0) = v_0$ (magenta thin-dotted line) is given on the upper axis.

We find that the dependence on the initial \ddot{R}_s , which is 0 for all models shown in this figure, is very minor, so we do not show its dependence here. In these calculations, $M_s(t = 0) = 0$, which is the mass below $R_s(0)$, is assumed to be a compact object and does not contribute to the mass of the shell. The almost constant velocity is a consequence of the density structure, $\rho_0(r) \propto r^{-\beta}$, with $\beta \approx 2$. The grey dotted line in the bottom panel represents the free-fall time-scale, $t_{\text{ff}} = \sqrt{R_s^3/G(M_c + M_s)}$, for the corresponding radius.

Fig. 2 gives the temperature in the expanding shell as a function of mass coordinate for the same model as in Fig. 1. The electron fraction in the iron core ($M \lesssim 1.55 M_\odot$) is less than 0.49 so that no ^{56}Ni production is expected. The maximum temperature of each mass element is determined by the energy injected until the shock front reaches the mass element. Thus, in order to achieve

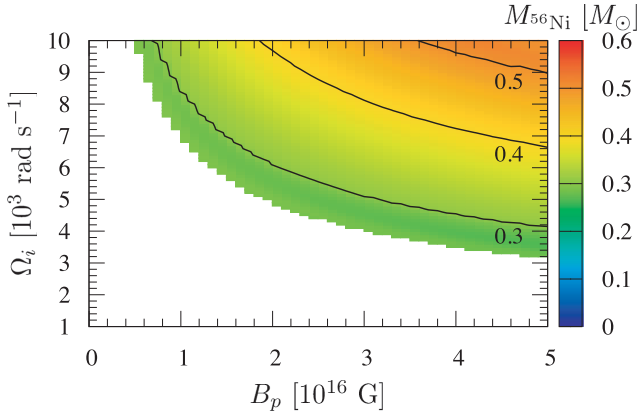


Figure 3. The amount of ^{56}Ni in units of M_{\odot} for the magnetar model as a function of the strength of the dipole magnetic field, B_p , and the initial angular velocity, Ω_i . The region with $M < 1.55 M_{\odot}$ is not included because $Y_e < 0.49$ and no ^{56}Ni production is expected there. Black solid lines represent $M_{56\text{Ni}}$ from 0.3 to 0.5 M_{\odot} .

$T > 5 \times 10^9$ K just above the iron core, an initially fast shock wave or a shock injected deep inside is necessary. This is because smaller initial velocity leads to a smaller initial kinetic energy, and larger injection radius leads to shorter and smaller energy injection before the shock reaches a certain radius. We employ $R_s(0) = 850$ km and $\dot{R}_s(0) = v_0$ to evaluate the maximum amount of ^{56}Ni in the following calculation. Although the model with $R_s(0) = 850$ km and $\dot{R}_s(0) = 0$ represents similar temperature, its expansion time of the shell is comparable to the free-fall time even for $L_w = 10^{52}$ erg s^{-1} (see Fig. 1), so that the explosion might fail.

Next, we consider the shock driven by the magnetar’s dipole radiation. Fig. 3 shows the ^{56}Ni mass produced in the expanding shell as a function of B_p and Ω_i . In this figure, we employ $R_{\text{NS}} = 10$ km and $I = 10^{45}$ g cm^2 . Here, we assume that the matter that experienced $T > 5 \times 10^9$ K is completely converted to ^{56}Ni , that is, $X(^{56}\text{Ni}) = 1$, except for $M(r) < 1.55 M_{\odot}$ where $Y_e < 0.49$. From this figure, we can easily see a rapid increase from 0 to $\sim 0.2 M_{\odot}$ of $M_{56\text{Ni}}$. In this progenitor, the silicon core has a mass of $\sim 1.84 M_{\odot}$, and the density slope β is different in the surrounding oxygen layer. This change in β causes the change of velocity evolution shown in Fig. 1: for instance, the blue thick-dashed line represents a rapid acceleration at $t \lesssim 0.5$ s and a slow acceleration or an almost constant velocity afterwards.

Because the observed brightness of HNe requires $\sim 0.2\text{--}0.5 M_{\odot}$ of ^{56}Ni (Nomoto et al. 2006), a reasonable central engine model must achieve this quantity. We find that for $M_{56\text{Ni}} \gtrsim 0.2 M_{\odot}$, the following relation should be satisfied:

$$\left(\frac{B_p}{10^{16} \text{ G}}\right)^{1/2} \left(\frac{\Omega_i}{10^4 \text{ rad s}^{-1}}\right) \gtrsim 0.68. \quad (15)$$

This condition can be derived by $E_{\text{NS}}/T_d \gtrsim 5.3 \times 10^{50}$ erg s^{-1} (see equations 4 and 5). Note that equation (15) is a conservative constraint because in this calculation we made several approximations, which always result in larger $M_{56\text{Ni}}$. Thus, for a more realistic case, $M_{56\text{Ni}}$ becomes smaller than this estimate. To make a reasonable amount of ^{56}Ni to explain the observation, a more energetic central engine is needed.

In order to investigate the progenitor dependence, we perform the same calculation with different progenitor models and find that the RHS of equation (15) is $\sim 0.64\text{--}0.90$: 0.68, 0.90 and 0.64 for the 20-, 40- and 80- M_{\odot} models of Woosley & Heger (2007),

respectively, and 0.71 for the 20- M_{\odot} model of Umeda & Nomoto (2005). Therefore, this criterion does not strongly depend on the detail of the progenitor structure. These calculations are performed with $M_c = M_{\odot}$ and $\dot{R}_s(0) = v_0$.

4 SUMMARY AND DISCUSSION

In this study, we employed the thin shell approximation for shock structure and calculated evolution of a shock wave driven by wind from a rapidly rotating NS with strong magnetic fields (i.e. magnetar). By evaluating temperature evolution that is consistent with the shock evolution, we obtained a constraint on the magnetar parameters, namely magnetic field strength and rotation velocity (see equation 15), for synthesizing enough ^{56}Ni to explain the brightness of HNe.

In this calculation, we employed several assumptions.

(i) The dipole radiation is dissipated between the NS and the shock, and thermal pressure drives the shock evolution. This assumption leads to a larger amount of ^{56}Ni than more realistic situations because, if the conversion from Poynting flux to thermal energy is insufficient, the internal energy is smaller and the temperature in the shell is lower than the current evaluation. Therefore, the mass that experienced $T > 5 \times 10^9$ becomes smaller.

(ii) The shock and energy deposition from the magnetar are spherical, which leads to larger ^{56}Ni mass. This is because fall-back of matter on to a NS takes place and reduces $M_{56\text{Ni}}$, if the explosion energy is concentrated in a small region (Bucciantini et al. 2009; Maeda & Tominaga 2009; Yoshida, Okita & Umeda 2014).

(iii) All energy radiated by the NS is used for the HN component, which is overestimated because a part of the energy should be used to make the relativistic jet component of a GRB.

(iv) The density inside the shell is assumed to be the same as the progenitor model. This assumption results in a higher temperature and larger $M_{56\text{Ni}}$ than realistic hydrodynamical calculations because the shock enhances not only the pressure but also the density in the shell.

(v) Matter that experiences $T > 5 \times 10^9$ K consists only of ^{56}Ni , i.e. $X(^{56}\text{Ni}) = 1$. This overestimates $M_{56\text{Ni}}$ because $X(^{56}\text{Ni}) < 1$, even in the layer that experiences $T > 5 \times 10^9$ K according to hydrodynamical and nucleosynthesis simulations (Tominaga et al. 2007).

(vi) The mass cut corresponds to the iron core mass, $1.55 M_{\odot}$. If the NS mass is larger than the iron core mass, the ^{56}Ni mass becomes even smaller.

(vii) The ram pressure is neglected in the evolutionary equation of the shell. According to the estimate of the shock propagation time and the free-fall time, in the low-luminosity case, the shell could not propagate outward for more realistic calculations.

Combining these facts, our estimation of the ^{56}Ni mass is probably highly overestimated so that our constraint on the magnetar parameters (equation 15) is rather conservative. Interestingly, it is still a stringent constraint; a very high magnetic field strength and a very rapid rotation are required to explain the brightness of HNe.

Next, we discuss more detailed MHD simulations for mechanisms driving ejecta by transferring rotational energy of magnetars using magnetic fields, although the mechanism is different from the dipole radiation assumed in this study. Bucciantini et al. (2009) performed MHD simulations around new-born magnetars from 1 s after supernova shock emergence. They found that the energy extracted from magnetars through magnetic fields is confined in the jet (directed flow) and the temperature cannot be high enough to

produce ^{56}Ni , even for the most energetic model in their study ($B = 3 \times 10^{15}$ G and $\Omega \approx 6000$ rad s $^{-1}$). More recently, MHD simulations with detailed microphysics, which run from the onset of iron-core collapse to the explosion driven by magnetic fields, showed that the resultant ^{56}Ni amount was $\lesssim 0.04 M_{\odot}$ (Nishimura et al. 2015) for a model with $B \sim 10^{15}$ G and $\Omega \approx 3000$ rad s $^{-1}$ (found in Takiwaki, Kotake & Sato 2009, for hydrodynamic explanations of their models). Therefore, the amount of ^{56}Ni cannot be amplified even when we take into account such MHD-driven outflow.

There have been some studies that tried to explain the plateau phase of the early afterglow by the magnetar scenario, because the long-lasting activity can be explained by long-living magnetars. This discriminates the magnetar scenario from the collapsar scenario, whose lifetime is determined by the accretion time-scale of the hyperaccretion flow. The typical values for B_p and Ω_i for long GRBs are $\gtrsim 3 \times 10^{14}$ G and $\gtrsim 6 \times 10^3$ rad s $^{-1}$ (Troja et al. 2007) and $3.2\text{--}12 \times 10^{14}$ G and $1.7\text{--}6.3 \times 10^3$ rad s $^{-1}$ (Dall’Osso et al. 2011). These values are far less than those given by equation (15). Therefore, if these GRBs are actually driven by a magnetar, we cannot expect the bright emission of HNe generated by the decay of ^{56}Ni . When we observe a GRB accompanying a HN, whose early afterglow can be explained by a magnetar without fulfilling the constraint given by equation (15), we need an additional energy source to synthesize ^{56}Ni other than the dipole radiation from magnetars.

Because the magnetar scenario was recently suggested for the central engine of superluminous supernovae (SLSNe) (e.g. Kasen & Bildsten 2010; Woosley 2010; Gal-Yam 2012) as well as GRBs, our discussion is applicable to this class of explosion. For instance, Kasen & Bildsten (2010) proposed that $B_p \sim 5 \times 10^{14}$ G and $\Omega_i \sim 10^2\text{--}10^3$ rad s $^{-1}$ are required to power the light curve of SLSNe. Thus, if the magnetar powers SLSNe, the synthesis of ^{56}Ni (i.e. ^{56}Fe) is not expected. This is in contrast to a pair-instability SN that is an alternative model for SLSNe.

ACKNOWLEDGEMENTS

YS thanks E. Müller for comments and M. Suwa for proofreading. This study was supported in part by the Grant-in-Aid for Scientific Research (Nos. 25103511 and 23740157). YS was supported by JSPS postdoctoral fellowships for research abroad, MEXT SPIRE, and JICFuS. TN was supported by the World Premier International Research Center Initiative (WPI Initiative), MEXT, Japan.

REFERENCES

- Blinnikov S., Lundqvist P., Bartunov O., Nomoto K., Iwamoto K., 2000, *ApJ*, 532, 1132
 Bucciantini N., Quataert E., Metzger B. D., Thompson T. A., Arons J., Del Zanna L., 2009, *MNRAS*, 396, 2038
 Burrows A., Dessart L., Livne E., Ott C. D., Murphy J., 2007, *ApJ*, 664, 416
 Dall’Osso S., Stratta G., Guetta D., Covino S., De Cesare G., Stella L., 2011, *A&A*, 526, A121
 Dessart L., Burrows A., Livne E., Ott C. D., 2008, *ApJ*, 673, L43
 Freiburghaus C., Rembes J.-F., Rauscher T., Kolbe E., Thielemann F.-K., Kratz K.-L., Pfeiffer B., Cowan J. J., 1999, *ApJ*, 516, 381
 Gal-Yam A., 2012, *Science*, 337, 927
 Hjorth J., Bloom J. S., 2012, in Kouveliotou C., Wijers R. A. M. J., Woosley S., eds, *Gamma-Ray Bursts*. Cambridge Univ. Press, Cambridge, p. 169

- Kasen D., Bildsten L., 2010, *ApJ*, 717, 245
 Komissarov S. S., Barkov M. V., 2007, *MNRAS*, 382, 1029
 Koo B.-C., McKee C. F., 1990, *ApJ*, 354, 513
 Laubach D. D., Probstein R. F., 1969, *J. Fluid Mechanics*, 35, 53
 LeBlanc J. M., Wilson J. R., 1970, *ApJ*, 161, 541
 MacFadyen A. I., Woosley S. E., 1999, *ApJ*, 524, 262
 Maeda K., Tominaga N., 2009, *MNRAS*, 394, 1317
 Maeda K., Nakamura T., Nomoto K., Mazzali P. A., Patat F., Hachisu I., 2002, *ApJ*, 565, 405
 Meier D. L., Epstein R. I., Arnett W. D., Schramm D. N., 1976, *ApJ*, 204, 869
 Metzger B. D., Giannios D., Thompson T. A., Bucciantini N., Quataert E., 2011, *MNRAS*, 413, 2031
 Mösta P. et al., 2014, *ApJ*, 785, L29
 Nagataki S., Mizuta A., Sato K., 2006, *ApJ*, 647, 1255
 Nakamura T., Mazzali P. A., Nomoto K., Iwamoto K., 2001a, *ApJ*, 550, 991
 Nakamura T., Umeda H., Iwamoto K., Nomoto K., Hashimoto M., Hix W. R., Thielemann F.-K., 2001b, *ApJ*, 555, 880
 Nishimura N., Takiwaki T., Thielemann F.-K., 2015, preprint (arXiv:1501.06567)
 Nomoto K., Tominaga N., Tanaka M., Maeda K., Suzuki T., Deng J. S., Mazzali P. A., 2006, *Nuovo Cimento B Ser.*, 121, 1207
 Sawai H., Yamada S., Suzuki H., 2013, *ApJ*, 770, L19
 Shapiro S. L., Teukolsky S. A., 1983, *Black Holes, White Dwarfs, and Neutron Stars: The Physics of Compact Objects*. Wiley-Interscience, New York
 Symbalisty E. M. D., 1984, *ApJ*, 285, 729
 Takiwaki T., Kotake K., Sato K., 2009, *ApJ*, 691, 1360
 Thompson T. A., Chang P., Quataert E., 2004, *ApJ*, 611, 380
 Tominaga N., 2009, *ApJ*, 690, 526
 Tominaga N., Maeda K., Umeda H., Nomoto K., Tanaka M., Iwamoto N., Suzuki T., Mazzali P. A., 2007, *ApJ*, 657, L77
 Troja E. et al., 2007, *ApJ*, 665, 599
 Umeda H., Nomoto K., 2005, *ApJ*, 619, 427
 Usov V. V., 1992, *Nature*, 357, 472
 Whitworth A. P., Francis N., 2002, *MNRAS*, 329, 641
 Winteler C., Käppeli R., Perego A., Arcones A., Vasset N., Nishimura N., Liebendörfer M., Thielemann F.-K., 2012, *ApJ*, 750, L22
 Woosley S. E., 1993, *ApJ*, 405, 273
 Woosley S. E., 2010, *ApJ*, 719, L204
 Woosley S. E., Bloom J. S., 2006, *ARA&A*, 44, 507
 Woosley S. E., Heger A., 2007, *Phys. Rep.*, 442, 269
 Woosley S. E., Heger A., Weaver T. A., 2002, *Rev. Mod. Phys.*, 74, 1015
 Yoshida T., Okita S., Umeda H., 2014, *MNRAS*, 438, 3119

APPENDIX A: TEST CALCULATIONS

Here, we show the validity of our calculation by comparing our calculation with a hydrodynamic simulation. In this comparison, we employ magnetars with three different sets of B_p and Ω_i , injected at $M(r) = 1.45 M_{\odot}$ of the $20 M_{\odot}$ progenitor of Umeda & Nomoto (2005). In Fig. A1, we show the comparison of the passing time (top panel) and the maximum temperature (bottom panel) as a function of mass coordinate for the shell calculation and the hydrodynamic simulation (Tominaga et al. 2007). The shock and temperature evolutions computed with these different methods agree quite well and the systematic error of our thin shell approximation for ^{56}Ni mass is $\sim O(0.01) M_{\odot}$, which is smaller than the characteristic amount of ^{56}Ni of HNe, $O(0.1) M_{\odot}$.

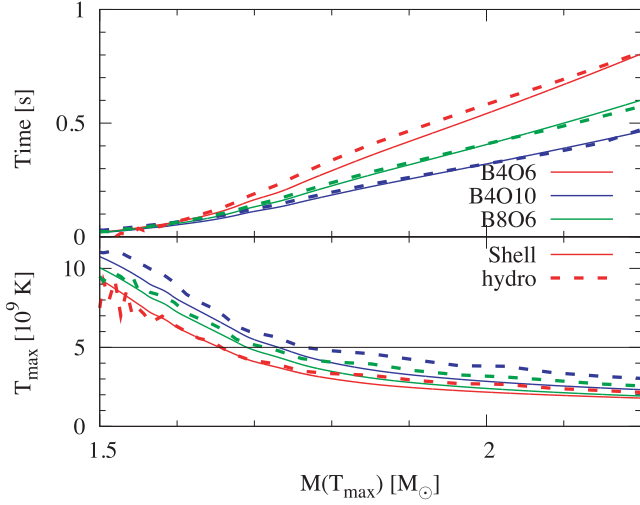


Figure A1. The passing time (top panel) and maximum temperature (bottom panel) for the shock as a function of mass coordinate. Solid and dotted curves represent the results of shell approximation (this work) and a hydrodynamic simulation, respectively. Colours represent magnetar parameters, $B = 4 \times 10^{16}$ G and $\Omega_i = 6000$ rad s^{-1} (red), $B = 4 \times 10^{16}$ G and $\Omega_i = 10^4$ rad s^{-1} (blue) and $B = 8 \times 10^{16}$ G and $\Omega_i = 6000$ rad s^{-1} (green). The horizontal dashed line in the bottom panel represents the critical temperature for ^{56}Ni synthesis, 5×10^9 K.

This paper has been typeset from a $\text{\TeX}/\text{\LaTeX}$ file prepared by the author.